Applied Catalysis B: Environment and Energy 344 (2024) 123670

Contents lists available at ScienceDirect

Applied Catalysis B: Environment and Energy

journal homepage: www.elsevier.com/locate/apcatb

Spinel-covered interlayer MgO enhances the performance of $BiVO_4$ photocatalytic ammonia synthesis

Kaiyi Chen [a], Rongling Wang [a], Qiong Mei [a], Fei Ding [a], Hui Liu [c], Guidong Yang [d,*], Bo Bai [a], Qizhao Wang [a,b,**]

[a] School of Water and Environment, Key Laboratory of Subsurface Hydrology and Ecological Effects in Arid Region of Ministry of Education, Key Laboratory of Subsurface Hydrology and Ecological Effect in Arid Region of the Ministry of Education, Chang'an University, Xi'an 710054, China
[b] College of Chemistry and Chemical Engineering, Northwest Normal University, Lanzhou 730070, Gansu, China
[c] School of Metallurgy and Environment, Chinese National Engineering Research Center for Control & Treatment of Heavy Metal Pollution, Central South University, Changsha 410083, China
[d] School of Chemical Engineering and Technology, Xi'an Jiaotong University, Xi'an, Shaanxi 710049, China

ARTICLE INFO

Keywords:
Spinel
$BiVO_4$
MgO
Nitrogen reduction reaction
Photoelectrocatalytic

ABSTRACT

In order to respond to the call for low emissions and low energy consumption, photoelectrochemical (PEC) ammonia synthesis is used to replace the Haber-Bosch method of nitrogen reduction, and highly efficient photoelectrocatalysts were used to reduce the reaction energy barrier. In this paper, the interlayer MgO and base $BiVO_4$ were successfully compounded by a simple electrodeposition method, and the spinel MCo_2O_4 (M=Zn, Mn) was compounded on MgO/$BiVO_4$ by a hydrothermal method, forming a sandwich structure of MCo_2O_4/MgO/$BiVO_4$ (M=Zn, Mn). The research shows that the sandwich structure constructed by MgO as the intermediate layer can reduce the excessive surface defects of photocatalyst, effectively reduce the recombination of photogenerated charge, promote the directional migration and separation of photogenerated charge, and improve the photocurrent density and photoelectric conversion efficiency. MCo_2O_4 (M=Zn, Mn) is a nitrogen reduction cocatalyst, which forms a heterojunction with n-type $BiVO_4$ and inhibits the recombination of photogenerated electrons. The synergistic effect of MCo_2O_4(M=Zn, Mn) and MgO accelerates the surface charge transfer efficiency and enhances the photoelectricity ammonia synthesis efficiency. The PEC ammonia synthesis efficiency reached more than 30 μmol h^{-1} g_{cat}^{-1}, and the Faradaic efficiency(FE) is over 30%.

1. Introduction

Nitrogen is an important part of the biogeochemical cycle, which plays an important role in nature and human life [1,2]. Although the nitrogen content in the atmosphere accounts for about 78%, it cannot be directly utilized . Ammonia (NH_3) exists in the form of nitrogen-containing compounds and is an important chemical raw material for the preparation of fertilizers, medicines and fuels [3–5]. In addition, NH_3 can also be used as a carrier for energy storage due to its high energy density and high hydrogen content [6–8]. But today, the industrial synthesis of ammonia from nitrogen is still mainly based on the Haber-Bosch method, which consumes a lot of energy and releases a lot of greenhouse gases [9–11]. The hydrogen consumed in the Haber-Bosch process accounts for 3–5% of the world's annual natural gas consumption [12–14]. Because the Haber-Bosch method pollutes the ecosystems on which human beings depend, researchers have endeavored to develop a green and sustainable nitrogen fixation method with mild reaction conditions. In recent years, the application of electrochemistry and photochemistry to heterogeneous catalysts to realize nitrogen reduction has received increasing attention from researchers, benefiting from mild operating conditions and utilization of renewable energy sources [15–17]. However, photocatalysis suffers from insufficient reaction kinetics due to its large dependence on the band gap width of semiconductor catalysts, resulting in low reaction efficiency. Due to the influence of mass transfer and overpotential, electrocatalysis will lead to the failure of excellent performance of the catalyst.

* Corresponding author.
** Corresponding author at: School of Water and Environment, Key Laboratory of Subsurface Hydrology and Ecological Effects in Arid Region of Ministry of Education, Key Laboratory of Subsurface Hydrology and Ecological Effect in Arid Region of the Ministry of Education, Chang'an University, Xi'an 710054, China.
E-mail addresses: guidongyang@mail.xjtu.edu.cn (G. Yang), wangqizhao@163.com, qzwang@chd.edu.cn (Q. Wang).

https://doi.org/10.1016/j.apcatb.2023.123670
Received 20 October 2023; Received in revised form 22 December 2023; Accepted 26 December 2023
Available online 29 December 2023

Photoelectrocatalysis (PEC) can overcome the disadvantages and give paly to their advantages . In this work, nitrogen is converted to ammonia using PEC under mild and environmentally friendly conditions.

To date, various photoelectrocatalysts include metal oxide/sulfide/boron [18–21], g-C_3N_4 [22], Bi-based photocatalysts [23–26], Au NPS [27,28], etc. Despite these recent advances, it is still an ongoing challenge to develop efficient and stable catalysts . Bismuth-based materials have recently received great attention as PEC ammonia synthesis [29–31]. Monoclinic scheelite $BiVO_4$ is a typical n-type direct band gap semiconductor with a forbidden bandwidth of 2.4 eV and 2.9 eV for scheelite and zircon, respectively [32–35]. In recent years, $BiVO_4$ has made many contributions in PEC water splitting and pollutant degradation. However, there is little research on $BiVO_4$ in the field of PEC ammonia synthesis. And the photogenerated carrier recombination rate of pure $BiVO_4$ is still high, which greatly affects the PEC reaction efficiency. The ammonia synthesis performance will be greatly improved if the high carrier compound efficiency of $BiVO_4$ is solved, which is also the key to solve the PEC ammonia synthesis. Therefore, finding an effective method to reduce the recombination of photogenerated electron-hole pairs in $BiVO_4$ is the fundamental problem to be addressed in this work. The passivation layer acts as a protective layer to prevent Bi shedding and improve the stability of the material and can prevent photo-corrosion by preventing the transport of photogenerated holes to the interface between the photoelectrocatalyst and the reaction medium. As an extremely stable inorganic insulator, MgO has good hole blocking characteristics, which can reduce the charge recombination at the interface of the composite electrode, and is a potential material for light transmission and barrier layer [36]. In addition, it is becoming a super-hydrophilic material because of the residual hydroxyl groups remaining on its surface [37]. Therefore, the presence of MgO passivation layer can inhibit photo-corrosion by accelerating the transfer of photogenerated hole . Spinel has a visible light response because of its narrow-forbidden band width and has the advantages of good thermal stability and rich elemental composition. In particular, the ternary spinel MCo_2O_4 (M = Ni, Mn, Zn, etc.) has better load-bearing conductivity and more active centers than Co_3O_4, resulting in a better nitrogen reduction capacity. However, MCo_2O_4 has mostly been used to study hydrolysis, but rarely in ammonia synthesis.

Herein, MCo_2O_4/MgO/$BiVO_4$(M = Zn, Mn) ternary composite photoanodes was used as photoanode to synthesize ammonia in H type reactor which platinum sheets are used as photocathode. MgO is used as an intermediate layer to reduce the excessive surface defects of the photocatalyst, and the photo-excited electrons on $BiVO_4$ are conducted to MgO, which reduces the recombination of electron holes. MCo_2O_4 (M = Zn, Mn) and $BiVO_4$ form a heterojunction , which promotes the directional transport of electrons. The synergistic effect of MCo_2O_4(M = Zn, Mn) and MgO accelerates the efficiency of surface charge transfer and enhances the efficiency of photoelectric ammonia synthesis .

2. Experimental section

2.1. Materials

All the chemicals, including vanadyl acetylacetonate ($VO(acac)_2$), bismuth nitrate pentahydrate ($Bi(NO_3)_3{\cdot}5\ H_2O$), nickel nitrate hexahydrate ($Ni(NO_3)_3{\cdot}6\ H_2O$), cobalt nitrate hexahydrate ($Co(NO_3)_3{\cdot}6\ H_2O$), Zinc nitrate hexahydrate ($Zn(NO_3)_2{\cdot}6\ H_2O$), potassium iodide (KI) and magnesium nitrate hexahydrate ($Mg(NO_3)_2{\cdot}6\ H_2O$), Dimethyl sulfoxide and p-benzoquinone (99.0%) were analytical grade and used with no further purification. The water utilized during the entire trials and characterization was deionized (DI) water.

2.2. Preparation of MCo_2O_4/MgO/$BiVO_4$(M = Zn, Mn)

$BiVO_4$ and MgO/$BiVO_4$ electrode was prepared according to a previous reported method and can be found at supporting information. MCo_2O_4/MgO/$BiVO_4$(M=Zn, Mn) was prepared by the method of hydrothermal. In brief, $Zn(NO_3)_2{\cdot}6\ H_2O$ and $Co(NO_3)_2{\cdot}6\ H_2O$ (1:2) were initially dissolved into 50 mL of DI water. Subsequently, 3 mmol of urea and 3 mmol NH_4F were added into the solution, which was further stirred for 1 h. The mixture was then transferred into a 100 mL Teflon-lined autoclave, and the MgO/$BiVO_4$ electrode was placed upright in the autoclave. Then the autoclave was sealed and heated in an oven at 493 K for 6 h. After the oven had cooled down to room temperature, the glass sheet was taken out and dried at 60 ℃ ~ 80 ℃ to obtain $ZnCo_2O_4$/MgO/$BiVO_4$. Replace $Zn(NO_3)_2{\cdot}6\ H_2O$ with $Mn(NO_3)_2$ solution and follow the same steps to obtain $MnCo_2O_4$/MgO/$BiVO_4$.

2.3. Characterization

Scanning electron microscopy (SEM) images were obtained on a Hitachi Regulus 8100 scanning electron microscope (Japan). The crystal structures of the materials were investigated by X-ray diffraction (XRD, X′Pert PRO MPD, Panalytical). The X-ray photoelectron spectra (XPS) of the materials were measured using a PHI-5000 versaprobe III (Japan). The UV-Vis diffuse reflectance (DRS) properties of the materials were recorded on a UV-Vis spectrophotometer. (Agilent Cary 100). Transmission electron microscopy (TEM) was performed on a JEOL- TF30 microscope. Photoluminescence (PL) spectra were recorded on steady state and transient state fluorescence spectrometer (Edinburgh FLS1000), excited at 540 nm. A series of photoelectrochemical performance measurements were performed on an electrochemical workstation (CHI760E) using the standard three-electrode system, which was composed of working electrode ($BiVO_4$, MgO/$BiVO_4$, MCo_2O_4/MgO/$BiVO_4$ (M = Zn, Mn), Pt wire as the counter electrode, and Ag/AgCl electrode as the reference electrode.

2.4. PEC N_2 fixation measurements

In order to investigate the PEC activity of MCo_2O_4/MgO/$BiVO_4$ (M = Zn, Mn) composite electrode. The N_2 reduction measurements were carried out on a CHI 760E electrochemical station in H-type cell in which three-electrode system (Fig. 9). The illumination source was a xenon lamp simulating sunlight AM 1.5 G (100 mW/cm^2), and a 0.1 M KOH solution was used as the electrolyte. Before the nitrogen reduction reaction (NRR) test, the cathode electrolyte was purified with high-purity nitrogen (99.999%) at a flow rate of 50 mL min^{-1} for 0.5 h. Since the reaction rate may be unstable in the early stage, the samples were taken and tested after 2 h in this experiment in order to ensure the experimental accuracy. A steady flow rate of 20 mL of nitrogen was maintained throughout the 2 h of the reaction.

Quantification of Ammonia: The ammonia concentrations in the electrolyte were measured by the indophenol blue method. Please refer to previous reports for specific test procedures.

Quantification of Hydrazine: The concentration of hydrazine was quantified by the method of Watt and Chrisp. The details are as follows: after the photoelectrochemical synthesis of ammonia in the H-type reactor for 2 h, 5 mL electrolyte solution was taken from the cathode cell, and 5 mL indicator (5 para-(dimethylamino) benzaldehyde, 30 mL concentrated hydrochloric acid and 300 mL ethanol) was added to stand for 2 h to measure its absorbance at 455 nm.

Computational Equation: Faradaic efficiency (FE) is the ratio of the number of transferred electrons used to produce NH_3 to the total amount of electricity provided to the reaction by the electrochemical workstation, which reflects the occurrence of competitive reactions.FE can be calculated as follows:

$$FE = \frac{3 \times F \times C \times V}{17 \times Q}$$

Among them, F is the Faraday constant, and C×V is the molar number of ammonia generated in NRR, Q is the total charge in NRR.

3. Results and discussion

3.1. Structural characterization of catalysts

Fig. S1 shows the XRD patterns of $BiVO_4$, $MgO/BiVO_4$ and $MCo_2O_4/MgO/BiVO_4$ (M = Zn, Mn). The XRD pattern shows that the diffraction peaks of $BiVO_4$ conform to the standard diffraction peaks of the monoclinic scheelite crystal system (JCPDS No. 75–1867). The peaks of 18.7°, 19.0°, 28.9°, 30.5°, 34.5°, 40.2°, 46.7° and 47.3° can be attributed to the (101), (011), (121), (004), (200), (204) and (024) crystal planes of monocline scheelite $BiVO_4$. Compared with the glass substrate FTO, no other impurity peaks except $BiVO_4$ were detected. After compounding, the intensity of the diffraction peak at 43.2° is enhanced for the $MgO/BiVO_4$ and $ZnCo_2O_4/MgO/BiVO_4$, while the peak disappears for the $MCo_2O_4/MgO/BiVO_4$(M =Zn, Mn). This may be due to the amount of MCo_2O_4 (M = Zn, Mn) compound being too small to be detected.

The morphologies of pristine $BiVO_4$ $MgO/BiVO_4$, $MnCo_2O_4/MgO/BiVO_4$ and $ZnCo_2O_4/MgO/BiVO_4$ were investigated by SEM. Fig. 1a shows that the pristine BiOI film consists of vertically aligned nanosheets. Such a uniform and uncrowded arrangement of nanosheets benefits from the stability of electrodeposition. $BiVO_4$ has a worm-like structure with a smooth surface and an overall loose and porous surface, which is favorable for electron transport and transfer, as shown in Fig. 1b. After loading MgO, the surface of $BiVO_4$ appears as rough particles with larger particle size and obvious traces of encapsulation. After loading with spinel, the surface of $MnCo_2O_4$ appears flower shape, while $ZnCo_2O_4/MgO/BiVO_4$ shows coral-like with a larger radius, indicating that spinel is loaded around $MgO/BiVO_4$.

The TEM micrograph (Fig. 2) of the $MCo_2O_4/MgO/BiVO_4$(M = Zn, Mn) reveals that the edges of $BiVO_4$ are formed by MgO thin layer. The TEM image of $ZnCo_2O_4/MgO/BiVO_4$ (Fig2b) shows that there are lattice fringes of 0.31, 0.24 and 0.47 nm on the selected cross section, which are the anatase (−112) plane of $BiVO_4$, the (111) plane of MgO and the (111) plane of $ZnCo_2O_4$, respectively. Moreover, we also found that $BiVO_4$, MgO, and $MnCo_2O_4$ exist simultaneously on $MnCo_2O_4/MgO/BiVO_4$, the lattice fringes of 0.47, 0.24 and 0.20 nm correspond to the (101) plane of $BiVO_4$, the (111) plane of MgO and the (400) plane of $MnCo_2O_4$, respectively. The elemental color mappings obtained using the EFTEM are shown in Fig. 2e–k, confirming the presence of constituent elements in the $MCo_2O_4/MgO/BiVO_4$(M = Zn, Mn), such as Bi, Zn, Mg, Co and Mn. The EFTEM micrographs also reveal the above elements all uniform distribution on $MCo_2O_4/MgO/BiVO_4$(M = Zn, Mn).

X-ray photoelectron spectroscopy (XPS) measurements were performed on $MCo_2O_4/MgO/BiVO_4$ to detect its surface composition and chemical state. The binding energies of Bi $4f_{5/2}$ and Bi $4f_{7/2}$ are 164.6 eV and 159.4 eV [38,39], while the $V2p_{1/2}$ and $V2p_{3/2}$ orbital peaks locate at 524 and 517 eV [40,41], respectively(Fig. S2a and S2g). The O 1 s XPS spectra are shown in Fig. S2e and the inverse convolution curves can be fitted to three segments with binding energies around 532.03 eV, 531.1 eV and 529.9 eV, representing surface hydroxyl groups, M-O and Mg-O, respectively [36]. Concerning Mg 1 s spectra (Fig S2h), an intensive peak centered at around 1304.5 eV corresponds to the MgO overlayers. The Co 2p spectra shown in Fig. 3d have peaks at 796.9 and 783.0 eV, which can be attributedto Co $2p_{1/2}$ and Co $2p_{3/2}$, and peaks at 804.0.6 and 787.4 eV attributable to the satellite peaks. The Co $2p_{1/2}$ and Co $2p_{3/2}$ peaks both can be further fitted into two contributions, the binding energy at 796.5 eV, 781.5 eV and 797.4, 783.9 eV can be assigned to Co^{2+} and Co^{3+} in $MCo_2O_4/MgO/BiVO_4$ (M = Zn, Mn), respectively [42].

The high-resolution spectrum of Mn2p observed in Fig. S2e shows that the peaks of $Mn2p_{1/2}$ spin orbitals at binding energy 652.78 eV and $Mn2p_{3/2}$ spin orbitals at binding energy 641.68 eV correspond to Mn^{2+} signals, and the peaks of $Mn2p_{1/2}$ spin orbitals at binding energy 654.48 eV and $Mn2p_{3/2}$ spin orbitals at binding energy 643.58 eV

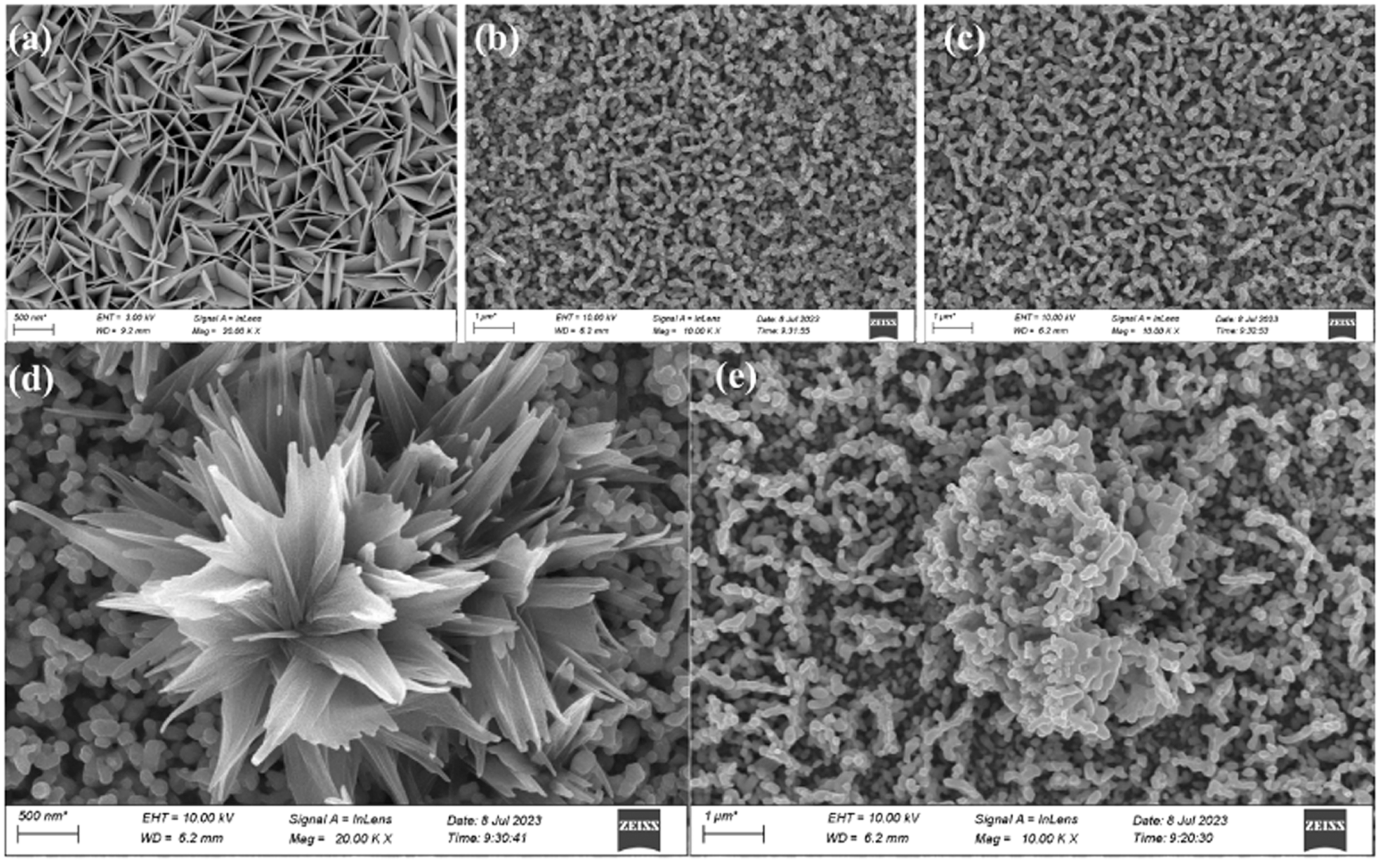

Fig. 1. SEM images of BiOI (a), $BiVO_4$ (b), $MgO/BiVO_4$ (c), $MnCo_2O_4/MgO/BiVO_4$(d) and $ZnCo_2O_4/MgO/BiVO_4$(e).

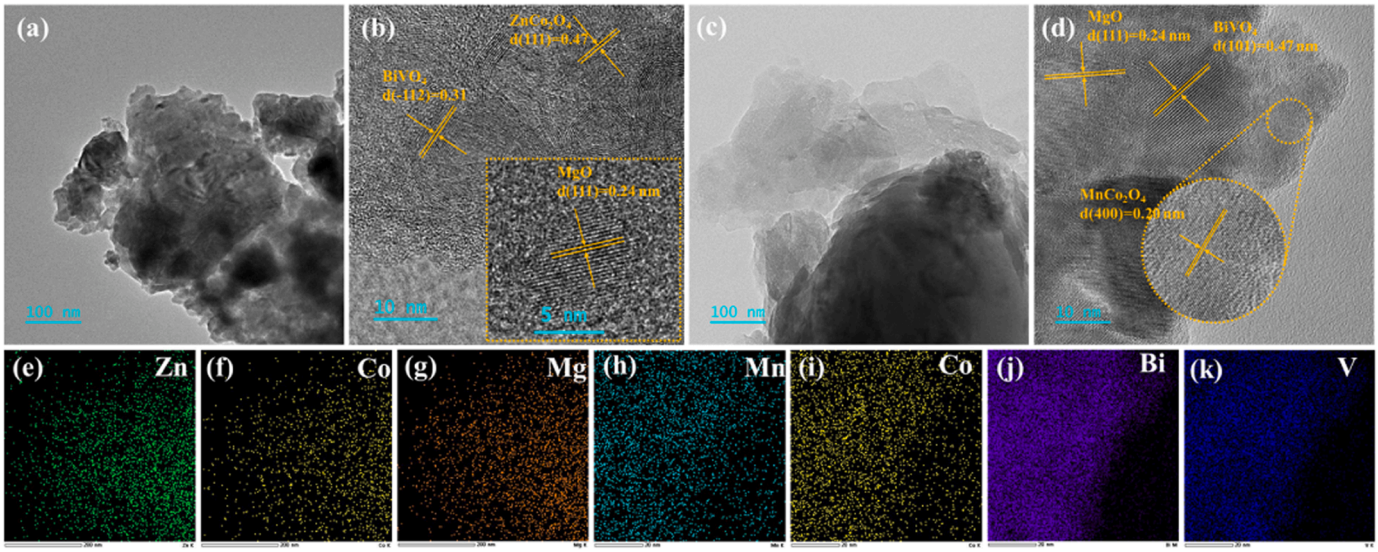

Fig. 2. TEM images of $ZnCo_2O_4$/MgO/$BiVO_4$(a, b), $MnCo_2O_4$/MgO/$BiVO_4$(c, d) and elemental mapping images of MCo_2O_4/MgO/$BiVO_4$(M=Zn, Mn) (e-k).

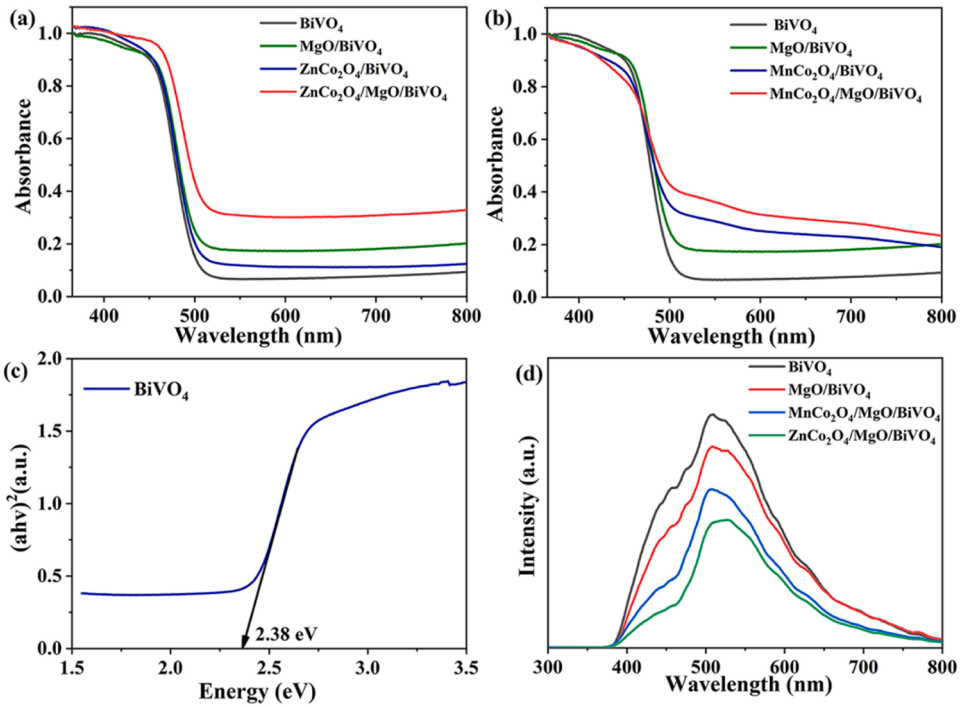

Fig. 3. (a)(b) UV–vis spectra of $BiVO_4$, MgO/$BiVO_4$, MCo_2O_4/$BiVO_4$ (M=Zn, Mn) and MCo_2O_4/MgO/$BiVO_4$ (M=Zn, Mn); (c) the energy gap of $BiVO_4$; (d) PL spectra of BiVO4, MgO/$BiVO_4$ and MCo_2O_4/MgO/$BiVO_4$ (M=Zn, Mn).

correspond to Mn^{3+} signals. This result indicates that manganese in $MnCo_2O_4$ is a mixed valence of Mn^{2+} and Mn^{3+} [43]. The binding energies of Zn $2p_{3/2}$ and Zn $2p_{1/2}$ peaks in the compound are located at 1021.1 eV and 1044.2 eV, respectively, indicating that Zn^{2+} existed in $ZnCo_2O_4$ compound. (Fig S2f) [38].

3.2. Optical properties and photocurrent response

The light absorption capacity is an important indicator for evaluating the photocatalytic performance of semiconductor materials. UV-Vis diffuse had used reflectance spectroscopy to systematically analyze the light absorption capacity of composite samples. It can be seen from Fig. 3a and b that the absorption edge of the pure $BiVO_4$ is about 500 nm. The red shift in the absorption edge of the MCo_2O_4/MgO/$BiVO_4$ (M = Zn, Mn) composite sample as the spinel is compounded, and the color of the prepared sample gradually deepens, which is consistent with the result. This indicates that the complex can use more light to excite the generation of photogenerated carriers, which in turn contributes to the PEC performance of the sample. Fig. 3c is the band gap value calculated by Tauc formula. The band gap value of $BiVO_4$ is 2.38 eV. Fig. 3d shows the PL of the $BiVO_4$, MgO/$BiVO_4$ and MCo_2O_4/MgO/$BiVO_4$(M = Zn, Mn) photoanodes at an excitation wavelength of 280 nm. The fluorescence intensity is highest for $BiVO_4$, followed by MgO/$BiVO_4$, and weaker for MCo_2O_4/MgO/$BiVO_4$(M = Zn, Mn) than for pure $BiVO_4$ and MgO/$BiVO_4$ films. This indicates that the photogenerated electron-hole pairs of the composite electrode are easier to

separate, so it has higher photon efficiency.

Fig. 4a and b show the LSV curves for the $BiVO_4$, $MCo_2O_4/BiVO_4$ (M = Zn, Mn), $MCo_2O_4/MgO/BiVO_4$ (M = Zn, Mn) photoanode. At 1.23 V vs. RHE, the photocurrent of BiVO4 is 1.45 mA cm^{-2} and the photocurrent densities of $MCo_2O_4/BiVO_4$ (M = Zn, Mn) are 4.13 mA cm^{-2} and 2.79 mA cm^{-2} respectively, which are 2.85 and 1.92 times higher than those of $BiVO_4$. The photocurrent densities of $MCo_2O_4/MgO/BiVO_4$ (M = Zn, Mn) are 4.595 mA cm^{-2} and 3.36 mA cm^{-2} respectively, which were 3.16 and 2.32 times higher than those of $BiVO_4$. The photocurrent density of the $MCo_2O_4/MgO/BiVO_4$ (M = Zn, Mn) composite electrode is much higher than that of the pure $BiVO_4$ film. This is mainly because the photogenerated holes are enriched on the surface of $BiVO_4$ films where a large amount of recombination of electron-hole pairs occurs. And when MgO is loaded on the $BiVO_4$ surface as an intermediate layer, the occurrence of hole accumulation can be effectively reduced. And MCo_2O_4 (M = Zn, Mn) inhibits the recombination of carriers during water oxidation, prolongs the carrier lifetime and improves the optical quantum efficiency. Ultimately, the photocatalytic performance was enhanced and the photocatalytic ammonia production was increased.

To further explore the photosensitivity of the $MCo_2O_4/MgO/BiVO_4$ (M = Zn, Mn) composite photoanode, an I-t curve (Fig. 4c and d) was made to represent the instantaneous photocurrent response of the composite electrode. Comparing the composite electrode with pure $BiVO_4$, the photocurrent density of the $MCo_2O_4/MgO/BiVO_4$ (M = Zn, Mn) composite electrode is much higher than that of the pure $BiVO_4$ film. This is mainly due to the large amount of electron-hole pair recombination that occurs on the surface of $BiVO_4$ thin films when photogenerated holes are enriched. And when MgO is used as a passivation layer to reduce the excessive surface defects of the photoelectrocatalyst, it can effectively reduce the photogenerated charge complex, promote the directional migration separation of photogenerated charges, increase the charge separation efficiency and improve the photocatalytic performance. MCo_2O_4 (M = Zn, Mn) forms a heterojunction with n-type $BiVO_4$ semiconductor, which is conducive to the separation of electron holes and can effectively reduce the occurrence of hole stacking conditions, Ultimately, the photocatalytic performance is enhanced and the photocatalytic ammonia yield is increased.

Fig. 5a shows electrochemical impedance spectroscopy (EIS) diagrams for $BiVO_4$, $MgO/BiVO_4$, $MCo_2O_4/BiVO_4$ (M = Zn, Mn) and $MCo_2O_4/MgO/BiVO_4$ (M = Zn, Mn) thin film samples. EIS is used to test the behaviors of charge transport at the photoanode phase or interface by applying a sinusoidal perturbation voltage to the photoanode. As shown in Fig. 5a, the size of the radius provides us with a direct indication of the strength of the photoelectrochemical activity of the photoanode. The smaller the radius, the faster the photoanode phase or interfacial charge migrates and the better the photoelectric performance. In agreement with the results of the LSV and I-t analyses, the photogenerated electron-hole pair separation efficiency of the composites is higher than that of the pure $BiVO_4$ electrode under both light conditions. This indicates that the faster the carrier transport rate of the electrode material, the lower the photogenerated electron and hole recombination rate. The LSV and EIS of $BiVO_4$, $MgO/BiVO_4$, $MnCo_2O_4/MgO/BiVO_4$ and $ZnCo_2O_4/MgO/BiVO_4$ under dark conditions are shown in Fig. S5. In the darkness, the onset potentials of $BiVO_4$, $MgO/BiVO_4$, $MnCo_2O_4/MgO/BiVO_4$ and $ZnCo_2O_4/MgO/BiVO_4$ were shifted back to 1.2 V vs. RHE. Nevertheless, the composite of MgO makes the onset potential of $BiVO_4$ low. The onset potential of $ZnCo_2O_4/MgO/BiVO_4$ is the smallest. The radius of the EIS diagram tested under dark conditions is much larger than that of the EIS diagram tested under light conditions. Nevertheless, the EIS plots of $MnCo_2O_4/MgO/BiVO_4$ and $ZnCo_2O_4/MgO/BiVO_4$ still show a smaller radius, showing that the impedance value are smaller.

LHE reflects the absorption and utilization of light by the catalytic electrode. In the range of 560.8–600 nm, the LHE of $ZnCo_2O_4/MgO/BiVO_4$ increased considerably to about 50.3%, and in the range of 375–560.8 nm, the LHE of $ZnCo_2O_4/MgO/BiVO_4$ continued to increase and finally reached 95.22% (Fig. S7). The charge separation efficiencies of $BiVO_4$, $MgO/BiVO_4$, $MnCo_2O_4/MgO/BiVO_4$, $ZnCo_2O_4/MgO/BiVO_4$ show a gradual increase in 0–1.3 V vs. RHE (Fig. S8). The charge

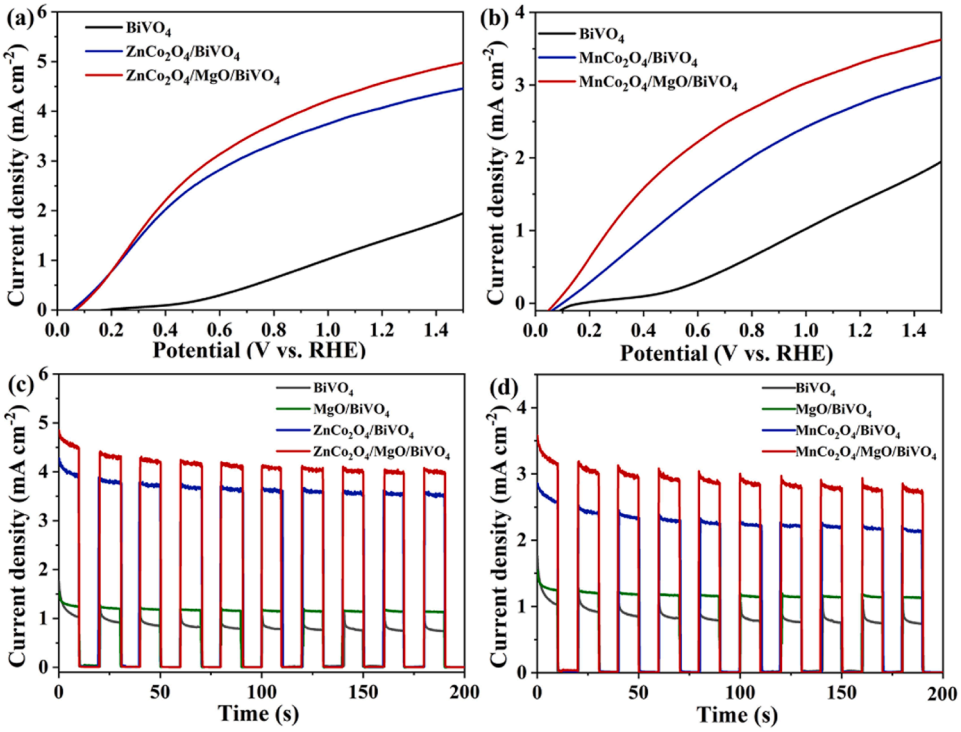

Fig. 4. LSV curves of $BiVO_4$, $ZnCo_2O_4/BiVO_4$ and $ZnCo_2O_4/MgO/BiVO_4$(a), $BiVO_4$, $MnCo_2O_4/BiVO_4$ and $MnCo_2O_4/MgO/BiVO_4$(b). Amperometric I-t curves of pure $BiVO_4$, $ZnCo_2O_4/BiVO_4$ and $ZnCo_2O_4/MgO/BiVO_4$(a), $BiVO_4$, $MnCo_2O_4/BiVO_4$ and $MnCo_2O_4/MgO/BiVO_4$.

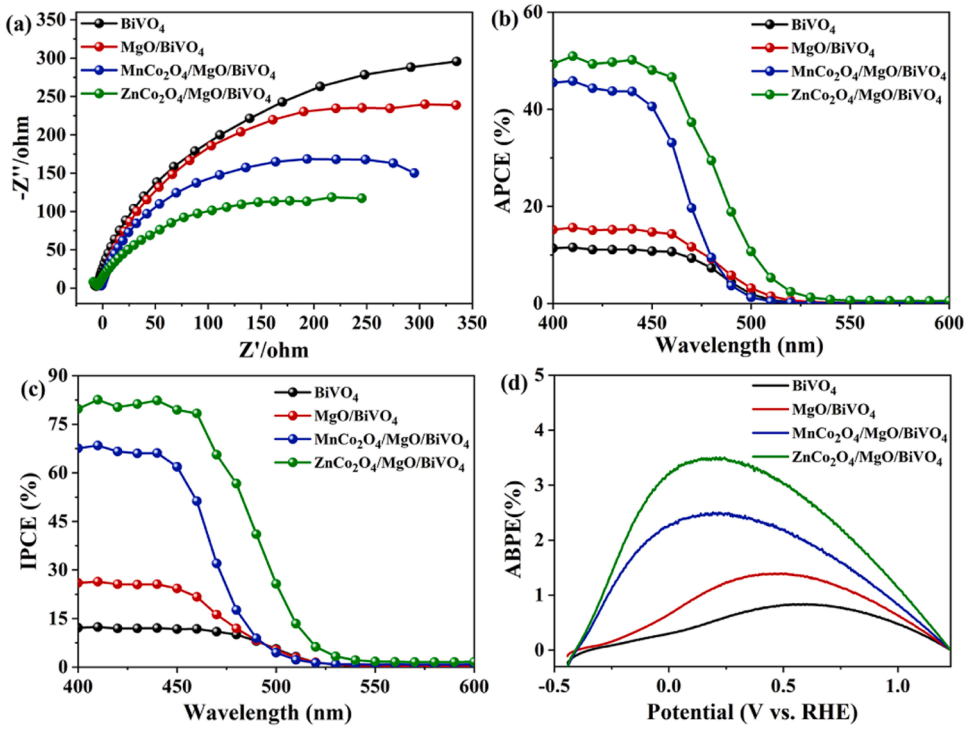

Fig. 5. EIS(a), APCE(b), IPCE(c) and ABPE(d) diagrams of $BiVO_4$, $MgO/BiVO_4$, $MCo_2O_4/BiVO_4$ (M = Zn, Mn) and $MCo_2O_4/MgO/BiVO_4$ (M = Zn, Mn).

separation efficiencies of $BiVO_4$, $MgO/BiVO_4$, $MnCo_2O_4/MgO/BiVO_4$, and $ZnCo_2O_4/MgO/BiVO_4$ at bias voltages of 1.23 V vs. RHE were 46.71%,54.31%, 60.48%, and 89.30%, respectively. The charge injection efficiency of $MnCo_2O_4/MgO/BiVO_4$ and $ZnCo_2O_4/MgO/BiVO_4$ remains above 60% and there is no obvious changes in a wide voltage range. The charge separation efficiencies of $BiVO_4$ and $MgO/BiVO_4$ slowly increase with increasing voltage. Eventually, the charge separation efficiency reaches up to 35% for $BiVO_4$ and 59% for $MgO/BiVO_4$. This illustrates the excellent electrochemical performance of $MnCo_2O_4/MgO/BiVO_4$ and $ZnCo_2O_4/MgO/BiVO_4$. The APCE, IPCE, ABPE values of $BiVO_4$, $MgO/BiVO_4$, $MCo_2O_4/BiVO_4$ (M = Zn, Mn) and $MCo_2O_4/MgO/BiVO_4$ (M = Zn, Mn) electrodes were measured in a 0.5 M Na_2SO_4 solution. The maximum APCE of $ZnCo_2O_4/MgO/BiVO_4$ and $MnCo_2O_4/MgO/BiVO_4$ reached 57% and 45.7% at 410 nm,

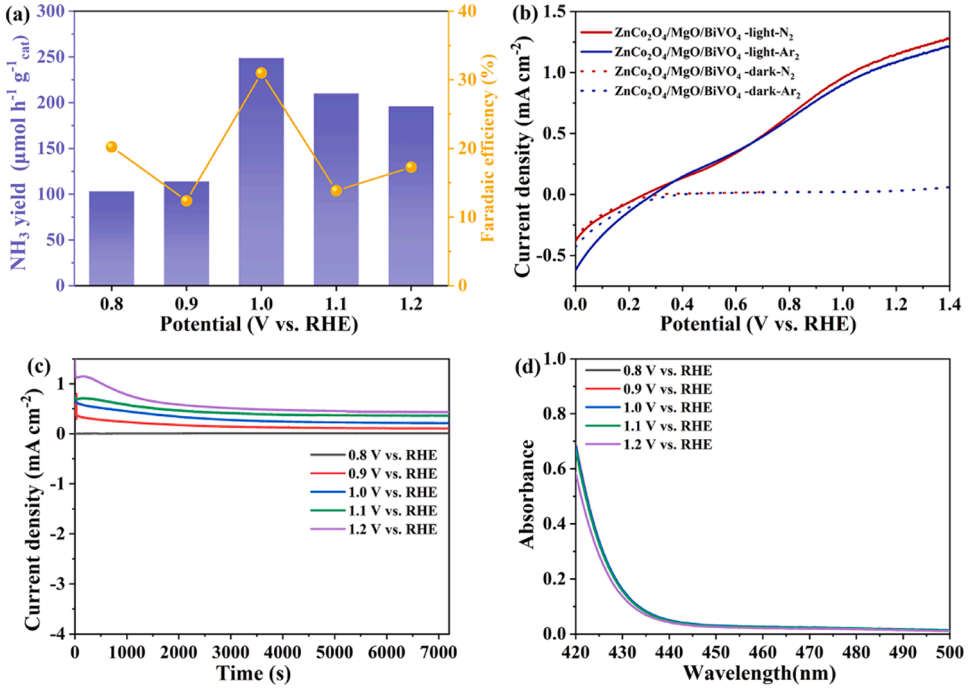

Fig. 6. (a) Ammonia formation rates (the average value on 2 h reaction) and corresponding Faradaic efficiencies of $ZnCo_2O_4/MgO/BiVO_4$, (b) Current−potential plots for $ZnCo_2O_4/MgO/BiVO_4$ light off, light on and N_2, Ar_2. (c) I-t curves of $ZnCo_2O_4/MgO/BiVO_4$ at various potentials, (d) UV–vis absorption spectrum for the electrolytes estimated by the Watt and Chrisp method (after being electrolyzed at −0.1 V vs. RHE for 2 h).

respectively (Fig. 5b), significantly higher than $BiVO_4$ (11.2% at 410 nm) and $MgO/BiVO_4$ photoanode (15.5% at 410 nm). The highest IPCE value of the $ZnCo_2O_4/MgO/BiVO_4$ and $MnCo_2O_4/MgO/BiVO_4$ electrodes reached 82.5% and 68.4% at 410 nm, respectively (Fig. 5c). This is marked improvement compared to $BiVO_4$ (12.3% at 410 nm) and $MgO/BiVO_4$ photoanode (26.4% at 410 nm). All these results provide further evidence that the photoelectric conversion efficiency of $MCo_2O_4/MgO/BiVO_4$ (M = Mn, Zn) in NRR is greatly improved. To assess the efficiency of the electrical energy being subtracted, ABPE was used as shown in Fig. 5d. $MnCo_2O_4/MgO/BiVO_4$, and $ZnCo_2O_4/MgO/BiVO_4$ achieve the highest efficiencies of 3.5% and 2.4% at 0.18 V, respectively, while MgO/BiVO4 $BiVO_4$ achieves the highest ABPE voltage with a significant backward shift. $MgO/BiVO_4$ can only obtain 1.4% at 0.46 V vs. RHE, and $BiVO_4$ can only obtain 0.8% at 0.59 V vs. RHE. Corresponds to the forward shift of the onset voltage of the $MCo_2O_4/MgO/BiVO_4$(M = Mn, Zn) LSV curve.

3.3. PEC NRR behaviors

Fig. 6a shows the performance of $ZnCo_2O_4/MgO/BiVO_4$ ammonia synthesis and Fig. 6b shows the current of the electrode tested in N_2, Ar saturated KOH solution in light and dark environment respectively. At 0.8 V vs. RHE and higher, the photocurrent of $ZnCo_2O_4/MgO/BiVO_4$ in N_2 saturated KOH solution is greater than that in Ar-saturated KOH solution, which indicates that the ternary composite electrode has better N_2 sensitivity at higher voltages. The currents of the ternary composite electrodes were all below 0.025 mA cm^{-2} in the dark environment, which is too small compared to the light conditions and shows the importance of light for the photoelectric response. We tested the performance of two ternary composite electrodes for ammonia synthesis over a wide voltage range, among which $ZnCo_2O_4/MgO/BiVO_4$ achieving the highest PEC ammonia synthesis performance (35.54 μmol h^{-1} g_{cat}^{-1}) and FE (30.99%) at 1.0 V vs. RHE. Fig. 6c shows the I-t profile of the electrode for ammonia synthesis at different voltages, which shows that the electrode has relatively good stability at lower voltages, with a reduction in photocurrent density of about 30% after two hours at 1.2 V vs. RHE. The current was highest at 1.2 V vs. RHE, however the ammonia yield and FE were relatively lower, probably due to competing reactions of hydrogen precipitation. $MnCo_2O_4/MgO/BiVO_4$ had the highest ammonia yield of 34.03 μmol h^{-1} g_{cat}^{-1} at 1.1 V vs. RHE (Fig. 7a) at a relatively low Faraday efficiency of 40.2%, while the highest Faraday efficiency was achieved 67.46% at 0.9 V vs. RHE, the increase in ammonia efficiency is accompanied by a competing reaction of hydrogen precipitation reactions. Fig. 7b shows the better N_2 sensitivity of $MnCo_2O_4/MgO/BiVO_4$ under 0.8–1.2 V vs. RHE light conditions. Fig. 7c shows the I-t profile of the electrode for the synthesis of ammonia at different voltages. $MnCo_2O_4/MgO/BiVO_4$ is more stable relative to $ZnCo_2O_4/MgO/BiVO_4$, showing better stability at 0.8–1.1 V vs. RHE and a 28% reduction in photocurrent density after two hours at 1.2 V vs. RHE. Figs. 6d and 7d show the UV–vis spectra of hydrazine hydrate tested by the Watt and Chrisp method two hours after the ammonia synthesis reaction of $MCo_2O_4/MgO/BiVO_4$(M = Mn, Zn), respectively. At the absorption peak of N_2H_4 at 455 nm, no intermediate hydrazine was formed in the ammonia synthesis reaction of $ZnCo_2O_4/MgO/BiVO_4$ and $MnCo_2O_4/MgO/BiVO_4$.

The efficiency of ammonia synthesis under different catalysts was compared , $BiVO_4$, $MgO/BiVO_4$, $ZnCo_2O_4/BiVO_4$ and $ZnCo_2O_4/MgO/BiVO_4$ were 6.34, 13.10, 17.13 and 35.52 μmol h^{-1} g_{cat}^{-1}, respectively at 1.0 V vs. RHE, FE of over 30% in all cases (Fig. 8a). The synthetic ammonia yield of $MnCo_2O_4/MgO/BiVO_4$ is 5.6 times that of $BiVO_4$. Ammonia synthesis tests were carried out at 1.1 V vs. RHE for $BiVO_4$, $MgO/BiVO_4$, $MnCo_2O_4/BiVO_4$, $MnCo_2O_4/MgO/BiVO_4$ with yields of 11.13, 17.14, 15.02 and 34.03 μmol h^{-1} g_{cat}^{-1}, respectively (Fig. 8b). $MnCo_2O_4/MgO/BiVO_4$ gives 3.06 times the yield of $BiVO_4$. Thereby, the ternary composite electrode has better photoelectric ammonia synthesis activity. Photoelectrochemical stability is crucial for further applications of catalysts. The ammonia synthesis rate and FE remained stable over five catalytic cycles of the H-cell (Fig. 8c and d), indicating the high electrochemical stability of $MCo_2O_4/MgO/BiVO_4$ (M = Mn, Zn). To illustrate the accuracy of experiment, the ammonia synthesis performance of $MnCo_2O_4/MgO/BiVO_4$ and $ZnCo_2O_4/MgO/BiVO_4$ in H-type electrolytic cell reactor for 2 h was tested by Ar (Fig.S9). After 2 h of

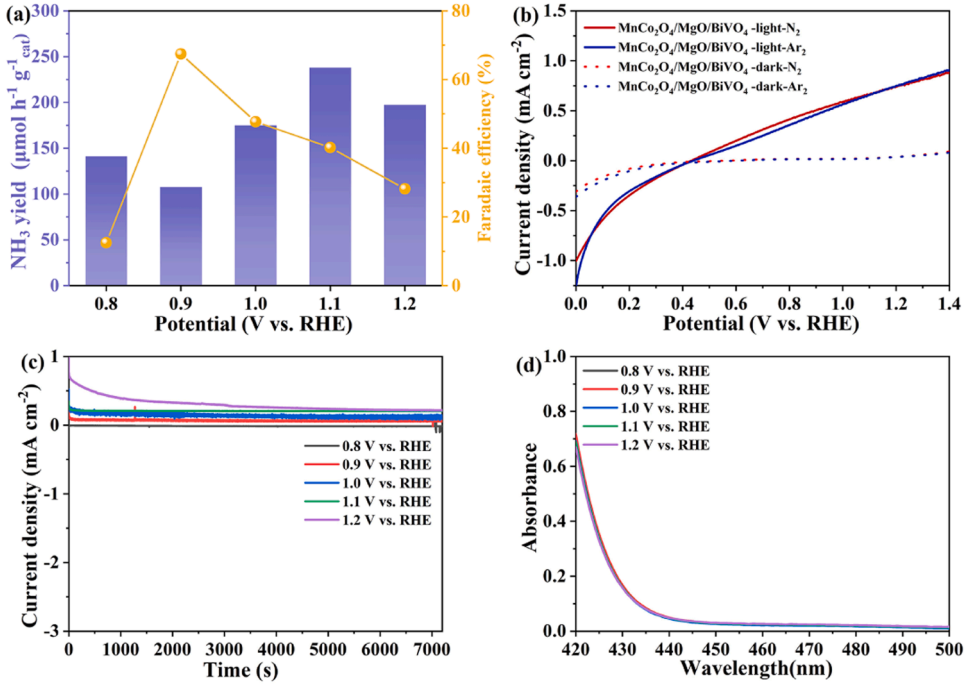

Fig. 7. (a) Ammonia formation rates (the average value on 2 h reaction) and corresponding Faradaic efficiencies of $MnCo_2O_4/MgO/BiVO_4$, (b) Current−potential plots for $MnCo_2O_4/MgO/BiVO_4$ light off, light on and N_2, Ar_2. (c) I-t curves of $MnCo_2O_4/MgO/BiVO_4$ at various potentials. (d) UV–vis spectra when in N_2H_4 measurements.

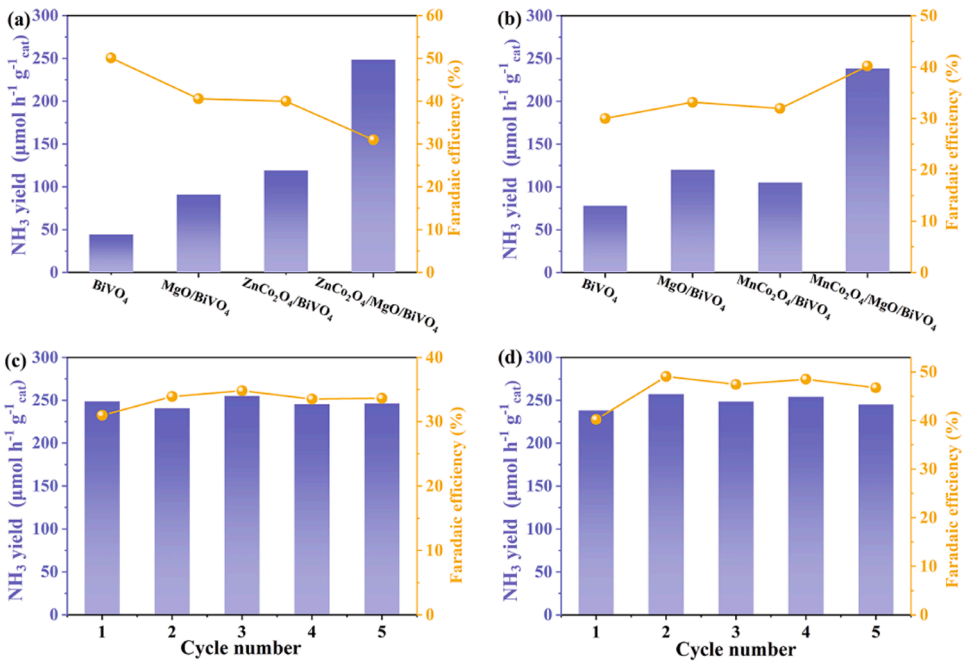

Fig. 8. (a) Average NH_3 yield rate and FE of $BiVO_4$, $MgO/BiVO_4$, $ZnCo_2O_4$/ $BiVO_4$ and $ZnCo_2O_4/MgO/BiVO_4$ at 1.0 V vs. RHE. (b) average NH_3 yield rate and FE of $BiVO_4$, $MgO/BiVO_4$, $MnCo_2O_4/BiVO_4$ and $MnCo_2O_4/MgO/BiVO_4$ at 1.1 V vs. RHE. (c) The stability test of $ZnCo_2O_4/MgO/BiVO_4$ for 5 cycles at 1.0 V vs. RHE in H cell. (d) The stability test of $MnCo_2O_4/MgO/BiVO_4$ for 5 cycles at 1.1 V vs. RHE in H cell.

ammonia synthesis, the NH_4^+ concentrations of $MnCo_2O_4/MgO/BiVO_4$ and $ZnCo_2O_4/MgO/BiVO_4$ catalysts in the cathode reaction cell were 2.18 and 1.34 μmol $h^{-1}g_{cat}^{-1}$, respectively. The FE were 1.03% and 0.99%, respectively. Therefore, all the N_2 for ammonia synthesis in the experiment originated from the gas supply cylinder, and the reaction system was well sealed without the interference of N_2 in the air(Fig. 9).

4. Conclusion

In this work, $MCo_2O_4/MgO/BiVO_4$(M = Zn, Mn) was successfully prepared by electrodeposition and hydrothermal strategy. Photochemical measurements show that the ammonia synthesis of $MCo_2O_4/MgO/BiVO_4$ (M = Zn, Mn) is greatly enhanced, and the ammonia synthesis efficiency of $ZnCo_2O_4/MgO/BiVO_4$ (35.52 μmol h^{-1} g_{cat}^{-1}) is higher than that of $MnCo_2O_4/MgO/BiVO_4$, but the FE is lower than that of $MnCo_2O_4/MgO/BiVO_4$(40.02%). I-t and cycling tests show that $MnCo_2O_4/MgO/BiVO_4$ (M=Zn, Mn) have good stability and provide a reliable idea for ammonia industrial grade applications.

CRediT authorship contribution statement

Wang Qizhao: Supervision, Writing – review & editing. **Wang Rongling:** Methodology, Writing – original draft. **Mei Qiong:** Data curation. **Chen Kaiyi:** Conceptualization, Methodology, Writing – original draft, Writing – review & editing. **Yang Guidong:** Supervision, Writing – review & editing. **Bai Bo:** Writing – review & editing. **Ding Fei:** Writing – review & editing. **Liu Hui:** Supervision, Writing – review & editing.

Declaration of Competing Interest

The authors declare that they have no known competing financial interests or personal relationships that could have appeared to influence the work reported in this paper.

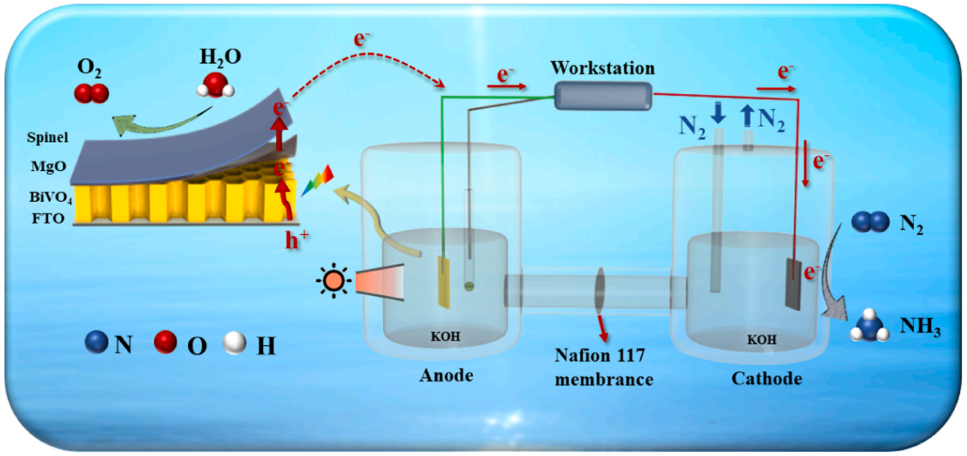

Fig. 9. Schematic diagram of PEC NRR mechanism and electron transfer process.

Data availability

Data will be made available on request.

Acknowledgments

This work was financially supported by the National Key Research and Development Program of China (2020YFA0710000), the National Natural Science Foundation of China (52173277), the Innovative Research Team for Science and Technology of Shaanxi Province (2022TD-04), the Fundamental Research Funds for the Central Universities of Chang'an University (300102299304), the Natural Science Basic Research Fund of Shaanxi Province (2020JZ-20).

Appendix A. Supporting information

Supplementary data associated with this article can be found in the online version at doi:10.1016/j.apcatb.2023.123670.

References

[1] J.W. Erisman, M.A. Sutton, J. Galloway, Z. Klimont, W. Winiwarter, How a century of ammonia synthesis changed the world, Nat. Geosci. 1 (2008) 636–639.
[2] M.M. Shi, D. Bao, B.R. Wulan, Y.H. Li, Y.F. Zhang, J.M. Yan, Q. Jiang, Au sub-nanoclusters on TiO_2 toward highly efficient and selective electrocatalyst for N_2 conversion to NH_3 at ambient conditions, Adv. Mater. 29 (2017) 1606550.
[3] X. Lv, F. Wang, J. Du, Q. Liu, Y. Luo, S. Lu, G. Chen, S. Gao, B. Zheng, X. Sun, Sn dendrites for electrocatalytic N_2 reduction to NH_3 under ambient conditions, Sustain. Energ. Fuels 4 (2020) 4469–4472.
[4] R. Schlögl, Catalytic synthesis of ammonia — a "never-ending story"? Angew. Chem. Int. Ed. 42 (2003) 2004–2008.
[5] L. Gao, H. Chai, H. Niu, J. Jin, J. Ma, Roles of cobalt-coordinated polymeric perylene diimide in hematite photoanodes for improved water oxidation, Small 19 (2023), e2302665.
[6] L. Li, C. Tang, D. Yao, Y. Zheng, S. Qiao, Electrochemical nitrogen reduction: identification and elimination of contamination in electrolyte, ACS Energy Lett. 4 (2019) 2111–2116.
[7] Y. Wang, Y. Yu, R. Jia, C. Zhang, B. Zhang, Electrochemical synthesis of nitric acid from air and ammonia through waste utilization, Natl. Sci. Rev. 6 (2019) 730–738.
[8] F. Niu, J. Zhu, Y. Ding, L. Tao, J. Jin, Energy bands matched photocatalysis enhancement based on viologen derivatives electron-transfer-mediator, Catal. Sci. Technol. 13 (2023) 1640–1649.
[9] C. Li, T. Wang, Z.J. Zhao, W. Yang, J.F. Li, A. Li, Z. Yang, G.A. Ozin, J. Gong, Promoted fixation of molecular nitrogen with surface oxygen vacancies on plasmon-enhanced TiO_2 photoelectrodes, Angew. Chem. Int. Ed. 57 (2018) 5278–5282.
[10] Z. Lu, B. Li, B. Wei, G. Zhou, Y. Xu, J. Zhang, H. Chen, S. Hua, C. Wu, X. Liu, NMP-induced surface self-corrosion-assisted rapid spin-coating method for synthesizing imprinted heterojunction photocatalyst anchored membrane towards high-efficiency selective degradation tetracycline, Sep. Purif. Technol. 314 (2023), 123609.
[11] K. Chen, X. Xu, Q. Mei, J. Huang, G. Yang, Q. Wang, Porous $TiWO_3/SrWO_4$ with high titanium molar ratio for efficient photoelectrocatalytic nitrogen reduction under mild conditions, Appl. Catal. B 341 (2024), 123299.
[12] L. Xia, B. Li, Y. Zhang, R. Zhang, L. Ji, H. Chen, G. Cui, H. Zheng, X. Sun, F. Xie, Q. Liu, Cr_2O_3 nanoparticle-reduced graphene oxide hybrid: a highly active electrocatalyst for N_2 reduction at ambient conditions, Inorg. Chem. 58 (2019) 2257–2260.
[13] X. Yan, D. Liu, H. Cao, F. Hou, J. Liang, S.X. Dou, Nitrogen reduction to ammonia on atomic-scale active sites under mild conditions, Small Methods 3 (2019) 1800501.
[14] Z. Lu, G. Zhou, B. Li, Y. Xu, P. Wang, H. Yan, M. Song, C. Ma, S. Han, X. Liu, Heterotopic reaction strategy for enhancing selective reduction and synergistic oxidation ability through trapping Cr (VI) into specific reaction site: a stable and self-cleaning ion imprinted CdS/HTNW photocatalytic membrane, Appl. Catal. B 301 (2022), 120787.
[15] X. Chen, N. Li, Z. Kong, W.J. Ong, X. Zhao, Photocatalytic fixation of nitrogen to ammonia: state-of-the-art advancements and future prospects, Mater. Horiz. 5 (2018) 9–27.
[16] S. Chen, S. Perathoner, C. Ampelli, C. Mebrahtu, D. Su, G. Centi, Electrocatalytic synthesis of ammonia at room temperature and atmospheric pressure from water and nitrogen on a carbon-nanotube-based electrocatalyst, Angew. Chem. Int. Ed. 129 (2017) 2743–2747.
[17] Y. Zhao, R. Shi, X. Bian, C. Zhou, Y. Zhao, S. Zhang, F. Wu, G.I.N. Waterhouse, L. Z. Wu, C.H. Tung, T. Zhang, Ammonia detection methods in photocatalytic and electrocatalytic experiments: how to improve the reliability of NH3 production rates? Adv. Sci. 6 (2019) 1802109.
[18] X. Zhang, T. Wu, H. Wang, R. Zhao, H. Chen, T. Wang, P. Wei, Y. Luo, Y. Zhang, X. Sun, Boron nanosheet: an elemental two-dimensional (2D) material for ambient electrocatalytic N_2-to-NH_3 fixation in neutral media, ACS Catal. 9 (2019) 4609–4615.
[19] (a) D. Zhu, L. Zhang, R.E. Ruther, R.J. Hamers, Photo-illuminated diamond as a solid-state source of solvated electrons in water for nitrogen reduction, Nat. Mater. 12 (2013) 836–841;
(b) Shuai Yue, Lu Chen, Manke Zhang, Zhe Liu, Tao Chen, Mingzheng Xie, Zhen Cao, Weihua Han, Electrostatic field enhanced photocatalytic CO_2 conversion on BiVO4 nanowires, Nanomicro Lett. 14 (2022) 1–12.
[20] C. Li, T. Wang, Z.-J. Zhao, W. Yang, J.F. Li, A. Li, Z. Yang, G.A. Ozin, J. Gong, Back cover: promoted fixation of molecular nitrogen with surface oxygen vacancies on plasmon-enhanced TiO_2 photoelectrodes, in: Angew. Chem. Int. Ed., 57, 2018, 5556-5556.
[21] Y. Bai, H. Bai, K. Qu, F. Wang, P. Guan, D. Xu, W. Fan, W. Shi, In-situ approach to fabricate BiOI photocathode with oxygen vacancies: understanding the N_2 reduced behavior in photoelectrochemical system, Chem. Eng. J. 362 (2019) 349–356.
[22] M.A. Mushtaq, M. Arif, X. Fang, G. Yasin, W. Ye, M. Basharat, B. Zhou, S. Yang, S. Ji, D. Yan, Photoelectrochemical reduction of N_2 to NH_3 under ambient conditions through hierarchical $MoSe_2$@ gC_3N_4 heterojunctions, J. Mater. 9 (2021) 2742–2753.
[23] C. Lv, C. Yan, G. Chen, Y. Ding, J. Sun, Y. Zhou, G. Yu, An amorphous noble-metal-free electrocatalyst that enables nitrogen fixation under ambient conditions, Angew. Chem. Int. Ed. 130 (2018) 6181–6184.
[24] (a) M. Ali, F. Zhou, K. Chen, C. Kotzur, C. Xiao, L. Bourgeois, X. Zhang, D. R. MacFarlane, Nanostructured photoelectrochemical solar cell for nitrogen reduction using plasmon-enhanced black silicon, Nat. Commun. 7 (2016) 11335;
(b) C. Zhou, J. Li, J. Wang, C. Xie, Y. Zhang, L. Li, T. Zhou, J. Bai, H. Zhu, B. Zhou, Efficient H_2 production and TN removal for urine disposal using a novel photoelectrocatalytic system of $Co_3O_4/BiVO_4$-MoNiCuOx/Cu, Appl. Catal. B 324 (2023), 122229.
[25] S. Wang, X. Hai, X. Ding, K. Chang, Y. Xiang, X. Meng, Z. Yang, H. Chen, J. Ye, Light-switchable oxygen vacancies in ultrafine Bi_5O_7Br nanotubes for boosting solar-driven nitrogen fixation in pure water, Adv. Mater. 29 (2017) 1701774.
[26] L. Wang, H. Cheng, Z. Zhang, Y. Zhang, J. Huang, H. She, C. Liu, Q. Wang, Rational design of honeycomb-like APTES-TiO_2/COF heterostructures: promoted intramolecular charge transfer for visible-light-driven catalytic CO_2 reduction, Chem. Eng. J. 456 (2023), 140990.
[27] Z. Zhang, S. Lindley, T. Chen, X. Cheng, E. Xie, W. Han, F. Toma, J.K. Cooper, Local charge transport at the interface of semiconductor and charge transport mediator, Adv. Opt. Mater. 10 (2022) 2201247.
[28] J. Zheng, Y. Lyu, M. Qiao, R. Wang, Y. Zhou, H. Li, C. Chen, Y. Li, H. Zhou, S. Wang, Photoelectrochemical synthesis of ammonia on the aerophilic-hydrophilic heterostructure with 37.8% efficiency, Chem 5 (2019) 617–633.
[29] J. Zhang, X. Wei, J. Zhao, Y. Zhang, L. Wang, J. Huang, H. She, Q. Wang, Electronegative Cl- modified $BiVO_4$ photoanode synergized with nickel hydroxide cocatalyst for high-performance photoelectrochemical water splitting, Chem. Eng. J. 454 (2023), 140081.
[30] D. Lee, W. Wang, C. Zhou, X. Tong, M. Liu, G. Galli, K. Choi, The impact of surface composition on the interfacial energetics and photoelectrochemical properties of $BiVO_4$, Nat. Energy 6 (2021) 287–294.
[31] (a) T. Zhou, S. Chen, L. Li, J. Wang, Y. Zhang, J. Li, J. Bai, L. Xia, Q. Xu, M. Rahim, B. Zhou, Carbon quantum dots modified anatase/rutile TiO_2 photoanode with dramatically enhanced photoelectrochemical performance, Appl. Catal. B 269 (2020), 118776;
(b) J. Su, L. Guo, N. Bao, C.A. Grimes, Nanostructured $WO_3/BiVO_4$ heterojunction films for efficient photoelectrochemical water splitting, Nano Lett. 11 (2011) 1928–1933.
[32] X. Hu, Q. Wang, Y. Li, Y. Meng, L. Wang, H. She, J. Huang, The hydrophilic treatment of a novel co-catalyst for greatly improving the solar water splitting performance over Mo-doped bismuth vanadate, J. Colloid Interface Sci. 607 (2022) 219–228.
[33] Y. Bai, J. Lu, H. Bai, Z. Fang, F. Wang, Y. Liu, D. Sun, B. Luo, W. Fan, W. Shi, Understanding the key role of vanadium in p-type $BiVO_4$ for photoelectrochemical N_2 fixation, Chem. Eng. J. 414 (2021), 128773.
[34] D. Jiang, L. Zhang, Q. Yue, T. Wang, Q. Huang, P. Du, Efficient suppression of surface charge recombination by CoP-Modified nanoporous $BiVO_4$ for photoelectrochemical water splitting, Int. J. Hydrog. Energy 46 (2021) 15517–15525.
[35] Y. Li, Q. Wang, X. Hu, Y. Meng, H. She, L. Wang, J. Huang, G. Zhu, Constructing NiFe-metal-organic frameworks from NiFe-layered double hydroxide as a highly efficient cocatalyst for $BiVO_4$ photoanode PEC water splitting, Chem. Eng. J. 433 (2022), 133592.
[36] H.W. Wang, J. Tian, W.B. Li, Electrochemical deposition of MgO@ZnO shell-core nanorod arrays largely enhances the photoelectrochemical water splitting performance, Chemelectrochem 4 (2017) 2019–2026.
[37] J. Cao, B. Wu, R. Chen, Y. Wu, Y. Hui, B.W. Mao, N. Zheng, Efficient, hysteresis-free, and stable perovskite solar cells with ZnO as electron-transport layer: effect of surface passivation, Adv. Mater. 30 (2018), 1705596.
[38] J. Huang, Y. Wang, K. Chen, T. Liu, Q. Wang, Boosting the photoelectrochemical water oxidation performance of bismuth vanadate by $ZnCo_2O_4$ nanoparticles, Chin. Chem. Lett. 33 (2022) 2060–2064.
[39] X. Shi, I.Y. Choi, K. Zhang, J. Kwon, D.Y. Kim, J.K. Lee, S.H. Oh, J.K. Kim, J. H. Park, Efficient photoelectrochemical hydrogen production from bismuth vanadate-decorated tungsten trioxide helix nanostructures, Nat. Commun. 5 (2014) 4775.

[40] D. Eisenberg, H.S. Ahn, A.J. Bard, Enhanced photoelectrochemical water oxidation on bismuth vanadate by electrodeposition of amorphous titanium dioxide, J. Am. Chem. Soc. 136 (2014) 14011–14014.
[41] H. Ren, T. Dittrich, H. Ma, J.N. Hart, S. Fengler, S. Chen, Y. Li, Y. Wang, F. Cao, M. Schieda, Y.H. Ng, Z. Xie, X. Bo, P. Koshy, L.R. Sheppard, C. Zhao, C.C. Sorrell, Manipulation of charge transport by metallic $V_{13}O_{16}$ decorated on bismuth vanadate photoelectrochemical catalyst, Adv. Mater. 31 (2019) 1807204.
[42] I.N. Demchenko, Y. Syryanyy, Y. Melikhov, L. Nittler, L. Gladczuk, K. Lasek, L. Cozzarini, M. Dalmiglio, A. Goldoni, P. Konstantynov, M. Chernyshova, X-ray photoelectron spectroscopy analysis as a tool to assess factors influencing magnetic anisotropy type in Co/MgO system with gold interlayer, Scr. Mater. 145 (2018) 50–53.
[43] D. Xu, T. Xia, H. Xu, W. Fan, W. Shi, Synthesis of ternary spinel MCo_2O_4 (M=Mn, Zn)/$BiVO_4$ photoelectrodes for photolectrochemical water splitting, Chem. Eng. J. 392 (2020), 124838.